Journal of Applied Physics

RESEARCH ARTICLE | AUGUST 01 1995

Raman scattering from anisotropic LO-phonon–plasmon–coupled mode in *n*-type 4H– and 6H–SiC

Hiroshi Harima; Shin-ichi Nakashima; Tomoki Uemura

J. Appl. Phys. 78, 1996–2005 (1995)
https://doi.org/10.1063/1.360174

Raman scattering from anisotropic LO-phonon–plasmon–coupled mode in *n*-type 4H– and 6H–SiC

Hiroshi Harima,[a] Shin-ichi Nakashima, and Tomoki Uemura
Department of Applied Physics, Osaka University, Yamadaoka 2-1, Suita 565, Japan

(Received 6 February 1995; accepted for publication 18 April 1995)

LO-phonon–plasmon–coupled modes in *n*-type 4H– and 6H–SiC single crystals with free-carrier concentrations of 10^{16}–10^{18} cm^{-3} have been measured by Raman scattering at room temperature. The axial-type mode for which plasma oscillation and atomic displacement are parallel to the *c* axis, and the planar-type mode for which these oscillations lie in the *c* plane, have been individually observed. From a line-shape analysis of the observed spectra, the plasmon frequency, carrier damping, and phonon damping have been deduced. These quantities have large differences between the axial- and planar-type mode in 6H–SiC, indicating its large crystal anisotropy. On the contrary, 4H–SiC shows small anisotropy. The longitudinal and transverse effective mass components of the electron have been determined from the plasmon frequency using carrier densities derived from Hall measurements. The deduced values are $m_{\parallel}=1.4m_0$ and $m_{\perp}=0.35m_0$ for 6H–SiC, and $m_{\parallel}=0.48m_0$ and $m_{\perp}=0.30m_0$ for 4H–SiC. The carrier mobility obtained from the analysis is also anisotropic. This is consistent with reported electrical measurements. © *1995 American Institute of Physics.*

I. INTRODUCTION

Silicon carbide (SiC) has received increased attention as a material for future high-temperature devices, high-voltage power-conditioning electronics, high-power microwave devices, etc., because of its advantage of high breakdown field, high saturated carrier velocity, and excellent thermal conductivity.[1] 6H–SiC, the most common polytype in silicon carbide, has actually been used for prototype devices such as power metal-oxide-semiconductor field-effect transistors (MOSFETs) and thyristers. Another polytype, 4H–SiC, has also shown high potential recently because its electron mobility is higher than that of 6H–SiC,[1,2] and has weaker anisotropy in electric transport properties.[2] Although there is a growing need for reliable data on the electronic properties of these hexagonal polytypes, many fundamental properties, such as the ionization energy of impurities and the effective mass of carriers, are not yet well known. Recently, IR-absorption spectra at low temperatures have been measured on *n*-type 6H–SiC and 4H–SiC crystals.[3,4] The observed absorption peaks were attributed to electronic transitions from the ground to excited states of nitrogen impurity levels, and anisotropic effective mass components of the electron were deduced from the binding energies of excited levels. Although the cyclotron resonance is a powerful technique for the direct determination of effective masses in semiconductors, such studies in silicon carbide have been limited to the cubic polytype, 3C–SiC.[5,6] Quite recently, however, Son *et al.* measured effective masses in 6H– and 4H–SiC by the optically detected cyclotron resonance (ODCR) technique,[7] which is less direct than the standard cyclotron resonance experiments. If we compare the effective masses, there are some marked differences among these recent data and previous experimental results.[3,4,7–10]

Raman scattering from LO-phonon–plasmon–coupled modes has been extensively studied in III–V semiconductors which have high carrier mobilities.[11] The plasmon frequency and carrier damping parameter were deduced from the analysis of the peak frequency and band shape of the coupled mode. This method was later applied to materials with relatively low carrier mobilities such as GaP,[12,13] ZnO,[14] ZnSe,[15] and 3C–SiC.[16] These experiments have demonstrated that carrier concentration and mobility derived from the band-shape analysis show reasonable agreement with those obtained from electrical measurements.

Recent rapid progress in the growth of 6H–SiC and 4H–SiC single crystals of good quality has motivated us to study their carrier transport properties systematically by Raman measurements of the LO-phonon–plasmon–coupled modes. Since these polytypes are uniaxial crystals, the electrical and phonon properties are expected to have anisotropy. In the present work we have observed the coupled mode with the following two scattering geometries; backscattering from the (0001) plane to observe the axial LO-phonon–plasmon–coupled mode (hereafter called as the axial coupled mode), and right-angle scattering with the incident- and scattered-light wave vectors perpendicular to the *c* axis to observe the planar LO-phonon–plasmon–coupled mode (the planar coupled mode). In the axial-type mode the directions of plasma oscillation and atomic displacement are parallel to the *c* axis, while in the planar-type mode they are perpendicular to the *c* axis.

We have analyzed the line shapes of the planar and axial coupled modes by fitting the theoretical band shape taking the plasmon frequency, carrier-, and phonon-damping rates as adjustable parameters. From the analysis, the effective masses of electrons have been deduced using the carrier concentrations determined by Hall measurements. Drift mobilities have also been obtained and compared with reported results of electrical measurements.

[a]Electronic mail: harima@ap.eng.osaka-u.ac.jp

 0021-8979/95/78(3)/1996/10/$6.00

Sections II and III describe the Raman experiment and the observed coupled mode profiles, respectively. In Sec. IV the fitting procedure is shown, and the electron effective masses as well as mobilities are deduced and compared with the results of previous measurements.

II. EXPERIMENT

Single crystals of 6H– and 4H–SiC with carrier concentrations ranging from 10^{16} to 10^{18} cm^{-3} were examined in this work. They were all grown by a modified Lely method. The c axis was determined by x-ray diffraction before cutting. The samples were shaped into rectangular parallelepipeds with faces perpendicular to the c axis. Single polytype samples having a spatially uniform carrier concentration and well-defined crystallographic axes were carefully selected. Boule SiC samples can often be highly stressed, which could introduce broadening and shift of spectral lines. We have selected only stress-free specimens by carefully observing the peak frequencies and width of strong TO-phonon bands (A_{1T} and E_{2T} modes, which are defined later). If the samples are highly stressed, these phonon peaks will show a discernible shift[17] from the reported peak frequencies.[18–20] Their carrier concentration was determined from the measurements of Hall coefficient R using the relation $n_H=r_H/|eR|$ under the assumption that the Hall factor r_H is unity. The uniformity of carrier concentration was confirmed by observing the coupled mode profiles at several different points on specimens by Raman microprobe.

Raman spectra of the coupled mode were obtained at room temperature using the Ar^+ laser line at 488 nm as the exciting source. The axial and planar coupled modes were observed in the backscattering geometry, $z(x,x+y)\bar{z}$, and in the right-angle scattering geometry, $x(z,x+z)y$, respectively, where $z \| c$ and $x,y \perp c$. The scattered light was collected by a camera lens onto a slit of a double monochromator, which had a focal length of 0.85 m and was equipped with a cooled charge-coupled device (CCD) detector. The observed spectra are not corrected for the distortions caused by the instrumental function deriving from the finite widths of the entrance slit (50 μm) and the CCD pixel element (23 μm). If the instrumental function is approximated by a trapezoid determined by these values, its spectral width [full width at half-maximum (FWHM)] is calculated as ~0.6 cm^{-1} from the reciprocal dispersion of the monochromator (about 12 cm^{-1}/mm in the observed spectral range). This is much smaller than the FWHM of the observed coupled modes (>3.5 cm^{-1}). Therefore, the distortions by the instrumental function could be neglected in the analysis. The Raman frequency was calibrated by a low-pressure neon lamp with known emission lines. The uncertainties in the Raman frequencies were estimated to be less than 1 cm^{-1}.

III. RESULTS

A. Coupled modes of 4H–SiC

Figure 1 shows typical Raman spectra for 4H–SiC crystals with carrier concentrations of $n_H=5.0\times10^{16}$ cm^{-3} and 1.3×10^{18} cm^{-3}. According to Raman selection rules for hexagonal SiC crystals (C_{6v}^4 space group),[18–20] the phonon

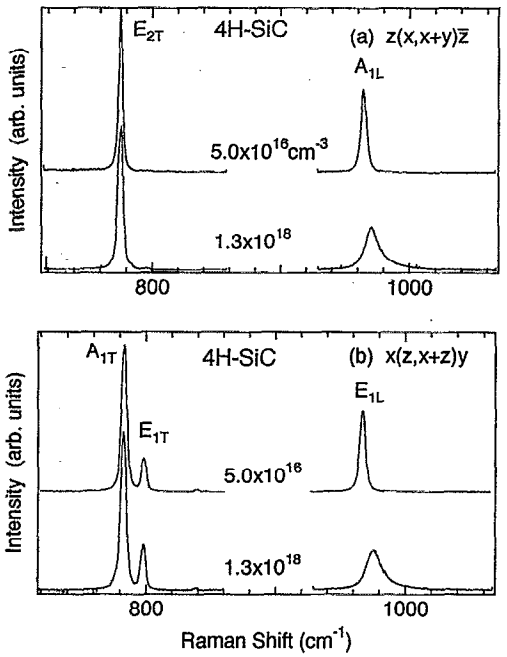

FIG. 1. Raman spectra of 4H–SiC with different carrier concentrations observed in (a) backscattering and (b) right-angle scattering geometries.

bands with A_1 symmetry (A_{1L} for LO phonon) and E_2 symmetry (E_{2T} for TO phonon) are allowed in the backscattering geometry $z(x,x+y)\bar{z}$ using the c face, while those with E_1 symmetry (E_{1L} and E_{1T}) and A_1 symmetry (A_{1T}) are allowed in the right-angle-scattering geometry $x(z,x+z)y$. As

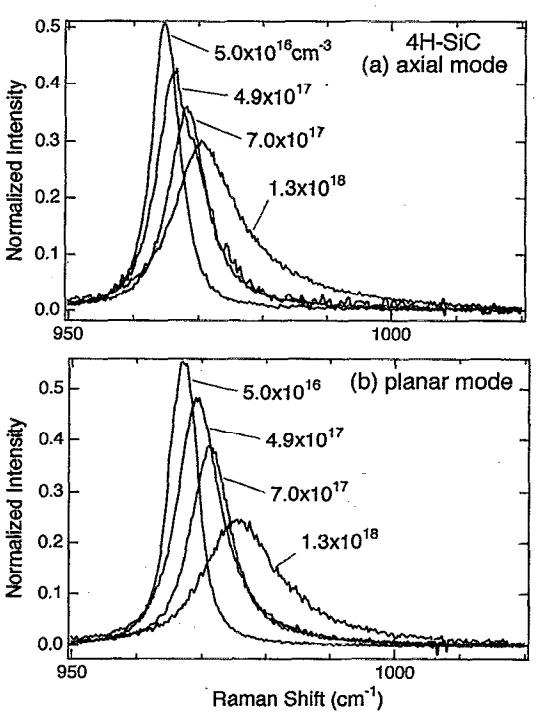

FIG. 2. Raman profiles of LO-phonon–plasmon–coupled mode for 4H–SiC with different carrier concentrations for (a) axial modes and (b) planar modes.

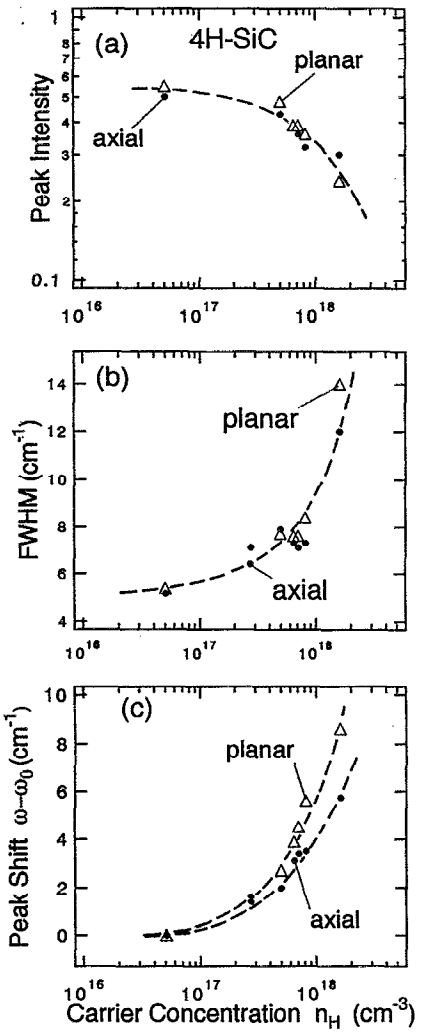

FIG. 3. (a) Peak intensity, (b) width (FWHM), and (c) peak shift of the coupled modes for 4H–SiC. The broken lines are drawn as a guide to the eyes. The peak shift is measured from the peak positions observed in the undoped sample with $n_H=5.0\times10^{16}$ cm^{-3}; 964.5 and 966.8 cm^{-1} for the axial and planar coupled mode, respectively.

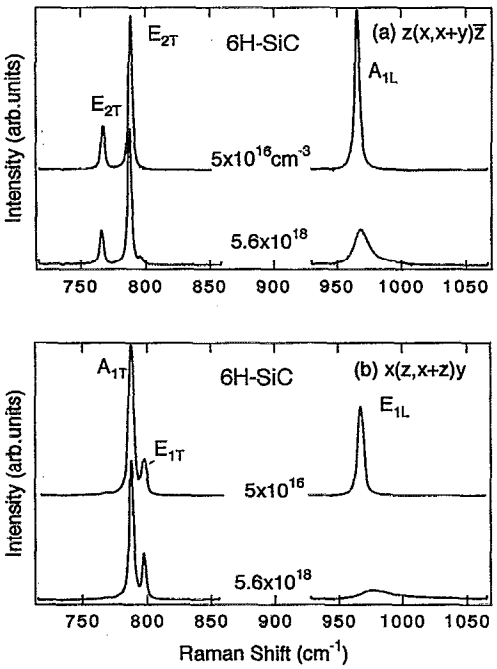

FIG. 4. Raman spectra of 6H–SiC with different carrier concentrations observed in (a) backscattering and (b) right-angle scattering geometries.

seen in this figure, the A_{1L}- and E_{1L}-band peaks located, respectively, at 964.5 cm^{-1} and 966.8 cm^{-1} in the undoped sample ($n_H=5.0\times10^{16}$ cm^{-3}) are broadened and shift to the higher-frequency side in the doped sample ($n_H=1.3\times10^{18}$ cm^{-3}). These bands correspond to the axial and planar coupled modes, respectively. On the contrary, the TO-phonon bands located at 776 cm^{-1} (E_{2T}), 783 cm^{-1} (A_{1T}), and 798 cm^{-1} (E_{1T}) are sharp (FWHM less than 3.5 cm^{-1}) and not affected by free carriers. These TO-phonon peak positions agree with published data[18–20] to within ±1 cm^{-1}.

Figure 2 shows the variation of the axial and planar coupled modes with the carrier concentration in more detail. Here the intensity of the axial coupled mode is normalized by the TO-phonon peak intensity (E_{2T}), and that of the planar coupled mode by the A_{1T}-phonon peak intensity. These profiles show typical features of LO-phonon–plasmon coupling: The peaks are broadened and shift to higher frequency as the carrier concentration increases. Figure 3 shows their peak intensity, width (FWHM), and peak shift against the carrier concentration n_H. Here, the peak shift is measured from the peak positions for the undoped sample with $n_H=5.0\times10^{16}$ cm^{-3}. There is no discernible difference in the peak intensity and width between the axial and planar coupled modes, while the planar coupled mode shows a larger peak shift than the axial coupled mode.

B. Coupled modes of 6H–SiC

Figure 4 shows typical spectra for the 6H–SiC samples with $n_H=5\times10^{16}$ cm^{-3} and 5.6×10^{18} cm^{-3}. The TO-phonon bands located at 767 and 789 cm^{-1} (both E_{2T} mode), 788 cm^{-1} (A_{1T}), and 797 cm^{-1} (E_{1T}) are not influenced by free carriers, in contrast to the axial (A_{1L}) and planar (E_{1L}) coupled modes. Figure 5 shows the variation of these coupled modes in more detail. Here, the intensity of the axial coupled mode is normalized by the peak intensity of the E_{2T} band at 789 cm^{-1}, and that of the planar coupled mode by the A_{1T}-phonon peak intensity. As seen clearly in this figure, the peak intensity of the planar mode decreases more strikingly than that of the axial mode with increasing the carrier concentration. Figure 6 shows their peak intensity, FWHM, and peak shift against the carrier concentration. Here the peak shift is measured from the peak positions for the undoped sample ($n_H=5\times10^{16}$ cm^{-3}); 964.5 and 969.8 cm^{-1} for the axial and planar coupled modes, respectively. The planar mode shows much larger variation than the axial mode in all these quantities, indicating that 6H–SiC has larger anisotropy than 4H–SiC.

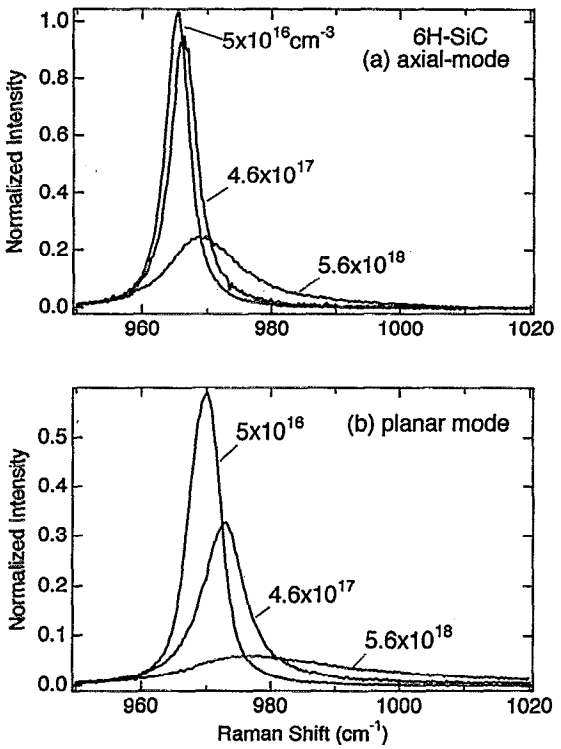

FIG. 5. Raman profiles of LO-phonon–plasmon–coupled mode for 6H–SiC with different carrier concentrations for (a) axial modes and (b) planar modes.

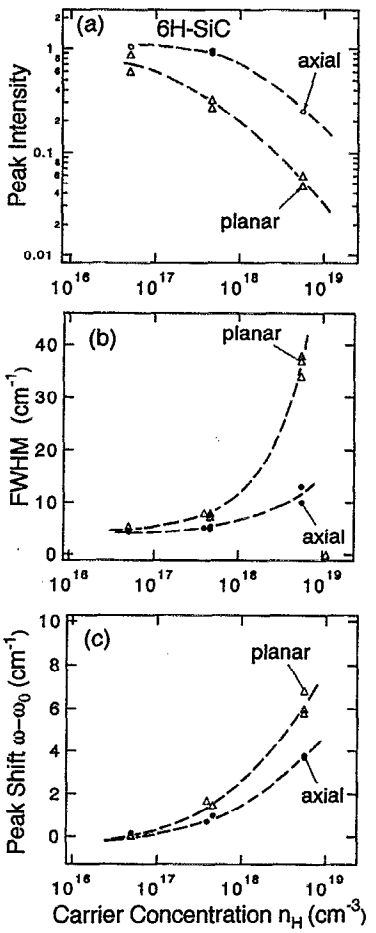

FIG. 6. (a) Peak intensity, (b) width (FWHM), and (c) peak shift of the coupled modes for 6H–SiC. The broken lines are drawn as a guide to the eyes. The peak shift is measured from the peak positions observed in the undoped sample with $n_H=5\times10^{16}$ cm^{-3}; 964.5 and 969.8 cm^{-1} for the axial and planar coupled mode, respectively.

IV. ANALYSIS AND DISCUSSION

A. Theoretical band shape

Raman scattering by the LO-phonon–plasmon–coupled mode in semiconductors with large band gap and low carrier mobility such as 6H–SiC,[21] GaP,[12,13] ZnO,[14] and 3C–SiC (Ref. 16) is dominated by a modulation of optical polarizability by atomic displacement (the so-called deformation-potential mechanism) and by a macroscopic longitudinal field (electro-optic mechanism), while the charge-density fluctuation mechanism plays a negligible role. Klein and co-workers[21] have shown that in this case the polarization selection rules for uncoupled LO phonons is valid also for the coupled modes. Figures 1 and 4 demonstrate that this prediction actually holds in our samples with carrier concentrations of 10^{16}–10^{18} cm^{-3}.

We first briefly review the theoretical treatment of the coupled mode for cubic crystals, then extend it to uniaxial or hexagonal systems. The Raman band profile of a coupled mode for cubic crystals is written as[12]

$$I(\omega)=SA(\omega)\mathrm{Im}[-1/\epsilon(\omega)], \tag{1}$$

where ω is the Raman shift, S is a proportionality constant, $\epsilon(\omega)$ is the dielectric function, and $A(\omega)$ is given by[12,16]

$$A(\omega)=1+2C\omega_T^2[\omega_p^2\gamma(\omega_T^2-\omega^2)-\omega^2\Gamma(\omega^2+\gamma^2-\omega_p^2)]/\Delta$$
$$+(C^2\omega_T^4/\Delta)\{\omega_p^2[\gamma(\omega_L^2-\omega_T^2)+\Gamma(\omega_p^2-2\omega^2)]$$
$$+\omega^2\Gamma(\omega^2+\gamma^2)\}/(\omega_L^2-\omega_T^2). \tag{2}$$

Here, ω_T and ω_L are the TO- and LO-phonon frequencies, respectively, γ is the plasmon damping constant, Γ is the phonon damping constant, and

$$\Delta=\omega_p^2\gamma[(\omega_T^2-\omega^2)^2+(\omega\Gamma)^2]+\omega^2\Gamma(\omega_L^2-\omega_T^2)(\omega^2+\gamma^2). \tag{3}$$

C is the so-called Faust–Henry coefficient,[22] which is related to the Raman-intensity ratio of LO- and TO-phonon bands in an undoped crystal by[11]

$$\frac{I_{\mathrm{LO}}}{I_{\mathrm{TO}}}=\left(\frac{\omega_1-\omega_L}{\omega_1-\omega_T}\right)^4\frac{\omega_T}{\omega_L}\left(1+\frac{\omega_T^2-\omega_L^2}{C\omega_T^2}\right)^2, \tag{4}$$

where ω_1 is the incident photon frequency. The dielectric function $\epsilon(\omega)$ is considered to be given by the contributions from phonons and plasmons,

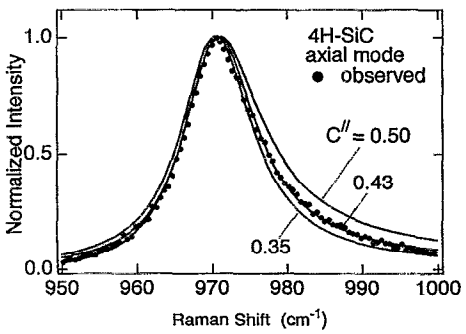

FIG. 7. Variation of theoretical line shape with the C coefficient. Observed profile for 4H–SiC with $n_H=1.3\times10^{18}$ cm^{-3} is shown by solid circles for comparison.

$$\epsilon(\omega)=\epsilon_\infty\left(1+\frac{\omega_L^2-\omega_T^2}{\omega_T^2-\omega^2-i\omega\Gamma}-\frac{\omega_p^2}{\omega(\omega+i\gamma)}\right). \tag{5}$$

The plasmon frequency ω_p is given by

$$\omega_p=\left(\frac{4\pi ne^2}{\epsilon_\infty m}\right)^{1/2}, \tag{6}$$

where ϵ_∞ is the optical dielectric constant, n is the concentration of free electrons, and m is the electron effective mass.

Next, we extend the above treatment to the hexagonal SiC crystals. Here we assume that the effective mass tensor is described only by two diagonal components $1/m_\parallel \equiv(1/m)_{zz}$ and $1/m_\perp\equiv(1/m)_{xx}=(1/m)_{yy}$, with the z direction parallel to the c axis. It means that the constant-energy surface at the conduction-band minima is given by a spheroid having the principal z axis along the c axis. In this case, the above equations (1)–(6) can be applied to axial and planar modes independently by defining the following different sets of parameters for the axial ($\parallel$) and planar ($\perp$) modes, respectively: TO-phonon frequency $\omega_T^{\parallel,\perp}$; uncoupled LO-phonon frequency $\omega_L^{\parallel,\perp}$; plasma frequency $\omega_p^{\parallel,\perp}$; damping rate of phonon $\Gamma^{\parallel,\perp}$; damping rate of plasmon $\gamma^{\parallel,\perp}$; Faust–Henry coefficient $C^{\parallel,\perp}$; and optical dielectric constant $\epsilon_\infty^{\parallel,\perp}$. The proportionality constant S takes different values for each mode.

If we make a rigorous symmetry argument based on the proposed locations of the conduction-band minima,[20,23–28] two perpendicular mass components, m_{xx} and m_{yy} ($\neq m_{xx}$), can be considered; however, since the x and y directions are not distinguished in the present experiment, $m_\perp$ deduced in this work should be considered as an average of the transverse components m_{xx} and m_{yy}.

B. Fitting procedure

We have fitted Eq. (1) to the observed planar and axial coupled mode profiles individually using $\omega_p^{\parallel,\perp}$, $\gamma^{\parallel,\perp}$, and $\Gamma^{\parallel,\perp}$ as adjustable parameters. Attention has been paid in the fitting to reproducing

(i) the peak intensity, treating S as a proportionality constant which is independent of the carrier concentration;

(ii) the peak shift from the uncoupled LO-phonon frequency ω_L; and

(iii) the asymmetric band shape.

The fitting of peak intensity is quite important for the unique determination of the parameters. Other constants required in the calculation have been determined as follows.

The observed peak positions of A_{1T} and E_{1T} modes are used for the TO-phonon frequencies $\omega_T^{\parallel,\perp}$. Since the pure 6H– or 4H–SiC bulk samples with carrier concentrations below 10^{16} cm^{-3} are not available at present, we have estimated the uncoupled or pure LO-phonon frequencies $\omega_L^{\parallel,\perp}$ from the fitting analysis of the coupled mode profiles for the undoped samples with the lowest carrier concentration tested ($n_H=5\times10^{16}$ cm^{-3}). In this fitting, $\omega_L^{\parallel,\perp}$ have been treated as adjustable parameters. The deduced values for the uncoupled LO-phonon frequencies are $\omega_L^{\parallel}=964.2$ cm^{-1} and $\omega_L^{\perp}=966.4$ cm^{-1} for 4H–SiC, and $\omega_L^{\parallel}=964.2$ cm^{-1} and $\omega_L^{\perp}=969.4$ cm^{-1} for 6H–SiC. It indicates that the pure LO-phonon frequencies are shifted by 0.3–0.4 cm^{-1} to lower frequency from the observed coupled mode peaks for the undoped samples ($n_H=5\times10^{16}$ cm^{-3}). Feldman *et al.*[18] reported peak frequencies of the pure planar and axial modes of 6H–SiC as 964 and 970 cm^{-1}, respectively. These values are in good agreement with our result.

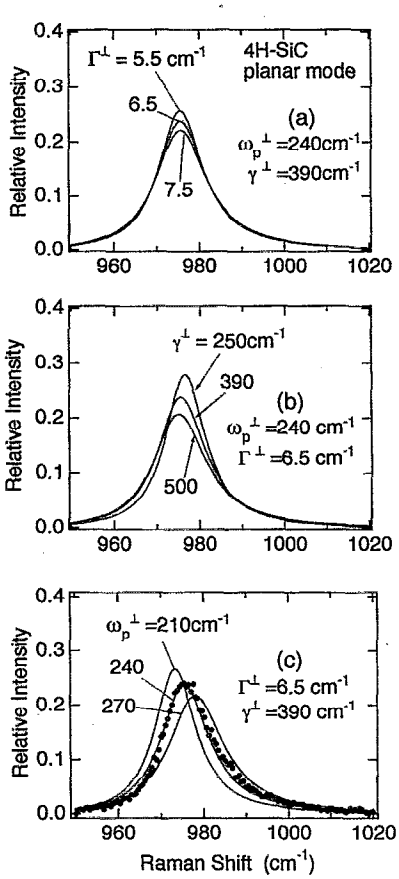

FIG. 8. Variation of theoretical line shape for the planar coupled mode with (a) phonon damping, (b) plasmon damping, and (c) plasmon frequency. Observed profile for 4H–SiC with $n_H=1.3\times10^{18}$ cm^{-3} is shown by solid circles for comparison.

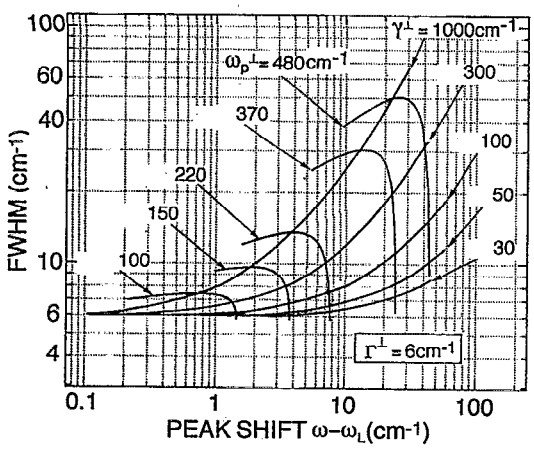

FIG. 9. Dependence of the peak shift and FWHM of theoretical line shape for the planar coupled mode on $\omega_p^{\perp}$ and $\gamma^{\perp}$ with $C^{\perp}=0.2$ and $\Gamma^{\perp}=6.0$ cm^{-1}.

Optical dielectric constants of $\epsilon_{\infty}^{\parallel}=6.70$ and $\epsilon_{\infty}^{\perp}=6.52$ are used for 6H–SiC.[29] These values are obtained by the extrapolation of refractive index data[30] in the visible region to low photon energy. For 4H–SiC we use $\epsilon_{\infty}^{\parallel}=6.78$ and $\epsilon_{\infty}^{\perp}=6.56$, which are deduced from the optical data of Shaffer[30] in the same manner.

To our knowledge, there is only a measurement of the Faust–Henry coefficient for α-SiC: By fitting of the coupled mode band shape observed in Raman scattering (488 nm excitation) to the theoretical line shape, Klein and co-workers[21] deduced $C^{\parallel}=0.39$ for the axial mode in a heavily doped 6H–SiC sample (nominal doping of 6×10^{19} cm^{-3}). In the present work the coefficient is determined as follows. In the right-angle scattering geometry employed here, the E_{1L} and E_{1T} modes are simultaneously observed as shown in Figs. 1(b) and 4(b). Therefore, the coefficient for the planar mode can be estimated from their intensity ratio in the undoped samples ($n_H=5\times10^{16}$ cm^{-3}) by using Eq. (4). We have obtained $C^{\perp}=0.20\pm0.03$ for 4H–SiC and 0.22 ± 0.03 for 6H–SiC. The Faust–Henry coefficient for the axial mode $C^{\parallel}$ has been determined by treating it as an adjustable parameter in the curve fitting for heavily doped samples, because the theoretical line shape at large carrier concentrations depends critically on the Faust–Henry coefficient. This feature is demonstrated in Fig. 7, in which the calculated profiles with different $C^{\parallel}$ values (solid lines) are compared with the observed profile for a 4H–SiC sample with $n_H=1.3\times10^{18}$ cm^{-3} (dotted line). The high-frequency tail grows with the increase of $C^{\parallel}$, though the peak position is scarcely affected. The best-fit values obtained are $C^{\parallel}=0.43\pm0.05$ for 4H–SiC, and 0.37 ± 0.05 for 6H–SiC. The latter value for 6H–SiC is close to the result of Klein and co-workers[21] Note the large anisotropy in the Faust–Henry coefficient (by a factor ~1.7–2.2) between the planar and axial modes in both polytypes. Such a large difference has been reported by Scott, Damen, and Shah[31] for CdS; $C^{\parallel}=0.50$ and $C^{\perp}=0.23$ at an excitation wavelength of 514.5 nm.

Figure 8 demonstrates the influence of phonon damping $\Gamma^{\perp}$, plasmon damping $\gamma^{\perp}$, and plasmon frequency $\omega_p^{\perp}$ on the planar coupled mode spectra. In Fig. 8(a) the observed profile for a 4H–SiC sample with $n_H=1.3\times10^{18}$ cm^{-3} is shown for comparison (dotted line). The phonon damping affects only the peak intensity and width as shown in Fig. 8(a), while the plasmon damping and plasmon frequency influence the peak position as well as the width and asymmetry as

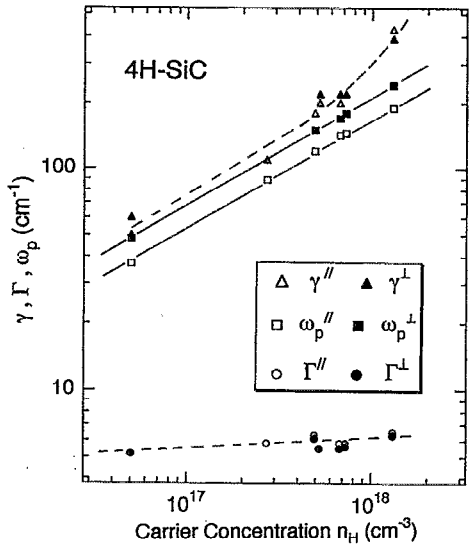

FIG. 11. Variation of the best-fit parameters γ, ω_P, and Γ for 4H–SiC with carrier concentration n_H. The solid lines show $n_H^{1/2}$ dependence. The broken lines are drawn to guide the eyes.

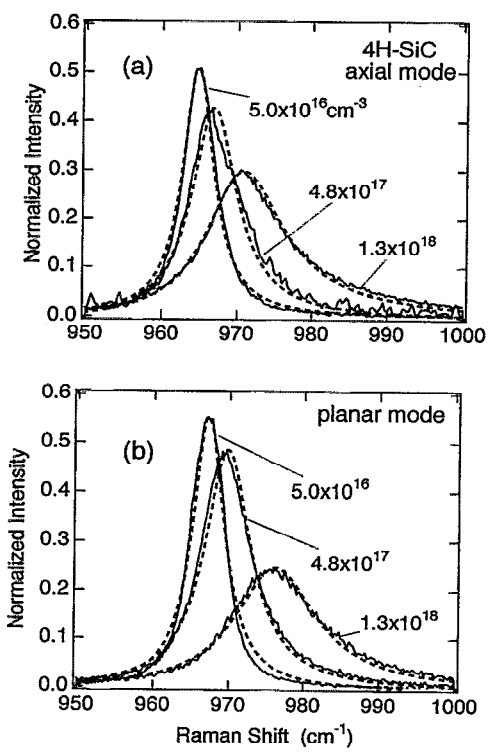

FIG. 10. Comparison between observed and calculated spectra for (a) axial and (b) planar coupled modes.

TABLE I. Best-fit parameters to coupled modes of 4H–SiC.

	Axial mode			Planar mode		
Sample no.	(1)	(2)	(3)	(1)	(2)	(3)
n_H (cm^{-3})	5.0×10^{16}	4.9×10^{17}	1.3×10^{18}	5.0×10^{16}	4.9×10^{17}	1.3×10^{18}
ω_p (cm^{-1})	37	120	190	48	150	240
γ (cm^{-1})	50	180	430	70	220	390
Γ (cm^{-1})	5.2	6.3	6.5	5.2	6.3	6.5
ω_L (cm^{-1})		964.2 (A_{1L})			966.4 (E_{1L})	
ω_T (cm^{-1})		783 (A_{1T})			798 (E_{1T})	
C		0.43			0.20	
ϵ_∞		6.78			6.56	

shown in Figs. 8(b) and 8(c). The width (FWHM) and shift from the uncoupled LO-phonon frequency $\omega_L^\perp$, calculated as functions of $\omega_p^\perp$ and $\gamma^\perp$ putting $C^\perp=0.2$ and $\Gamma^\perp=6$ cm^{-1}, are shown in the nomogram of Fig. 9. With the decrease of $\omega_p^\perp$ and $\gamma^\perp$, the peak frequency and width approach those of the uncoupled LO phonon.

The fitting was carried out as follows; $\gamma^{\parallel,\perp}$ and $\omega_p^{\parallel,\perp}$ were first roughly determined from the observed width and shift, referring to the result of simulations as shown in Fig. 9, then $\Gamma^{\parallel,\perp}$ was adjusted to fit the width. Finally, $\gamma^{\parallel,\perp}$ and $\omega_p^{\parallel,\perp}$ were adjusted again to reproduce the observed band shape (peak position, intensity, width, and asymmetry). When $C^\parallel$ was treated as the fitting parameter for the axial coupled mode, this coefficient was adjusted at first to obtain the fit to profiles for heavily doped samples.

C. Effective mass in 4H–SiC

Figure 10 shows typical results of fitting for 4H–SiC. The agreement of the experimental and calculated profiles is fairly good. The best-fit parameters, $\omega_p^{\parallel,\perp}$, $\gamma^{\parallel,\perp}$, and $\Gamma^{\parallel,\perp}$, for these profiles are listed in Table I together with other constants used. The carrier concentration n_H determined by Hall measurements is also shown in this table. The best-fit parameters are plotted against n_H in Fig. 11. With the increase of the carrier concentration, $\gamma^{\parallel,\perp}$ greatly increases, while $\Gamma^{\parallel,\perp}$ shows a slight increase. It should be noted that $\omega_p^{\parallel,\perp}$ increases proportionally to the square root of n_H for both the planar and axial modes as is expected from Eq. (6), if n_H is proportional to the real carrier concentration n. Thus, the Hall factor r_H can be treated as constant over the whole carrier-concentration range studied. In this work we have made the further assumption that r_H is unity. As seen in Fig. 11, the planar plasmon frequency $\omega_P^\perp$ is larger than that for the axial mode $\omega_P^\parallel$ by about 25%. If we refer to Eq. (6), this difference can be attributed to the anisotropy of electron effective mass, because the anisotropy of optical dielectric constant is very small ($\epsilon_\infty^\parallel=6.78$, $\epsilon_\infty^\perp=6.56$). Electron effective masses can be deduced from the best-fit plasma frequencies, using these dielectric constants and carrier concentrations obtained from Hall measurements: $m_\parallel/m_0=0.48\pm0.12$ and $m_\perp/m_0=0.30\pm0.07$ for 4H–SiC. In Table II these values are compared with other experimental results[4,7,9] and a theoretical calculation.[28] All the experimental data indicate that the effective masses range roughly $0.5-0.2m_0$. The remaining discrepancies among the data may be attributed to the variety of sample quality and assumptions used for analyses. In a recent *ab initio* band calculation, Käckell and co-workers[28] derived three independent mass components from the band curvature; they obtained a longitudinal mass $m_\parallel/m_0=0.39$ (along ML in the Brillouin zone), which agrees with our experimental result, and two transverse masses $m_\perp/m_0=0.62$ (along $M\Gamma$) and 0.13 (along MK). It is important to determine precisely the mass anisotropy $m_\perp/m_\parallel$, since it is deeply related to the anisotropy of carrier-transport properties.

TABLE II. Effective masses in 4H–SiC.

$m_\parallel/m_0$	0.48[a]	0.22[b]	0.19[c]	0.29[d]	0.39[e]
$m_\perp/m_0$	0.30[a]	0.18[b]	0.21[c]	0.42[d]	0.13, 0.62[e]

[a]This work; Raman scattering.
[b]Götz *et al.* (Ref. 4); IR absorption.
[c]Lomakina and Vodakov (Ref. 9); electrical conductivity.
[d]Son *et al.* (Ref. 7); optically detected cyclotron resonance.
[e]Käckell and co-workers (Ref. 28); band calculation.

D. Effective mass in 6H–SiC

The best-fit parameters for the 6H–SiC profiles shown in Fig. 5 are summarized in Table III together with other constants. The parameters show qualitatively the same dependence on n_H as in the case of 4H–SiC: $\gamma^{\parallel,\perp}$ greatly increases with increasing n_H, and $\omega_p^{\parallel,\perp}$ is proportional to $n_H^{1/2}$ for both the planar and axial modes. It is obvious from Table III that ω_p and γ have relatively large anisotropy and that the values for the planar mode are 2.1–2.3 times as large as those for the axial mode. The electron effective masses of 6H–SiC are highly anisotropic: $m_\parallel/m_0=1.4\pm0.3$ and $m_\perp/m_0=0.35\pm0.08$. As shown in Table IV, such a large anisotropy is in accordance with previous experimental results by Ellis and Moss,[8] Lomakina and Vodakov,[9] Mel'nichuk and Pasechnik,[10] and Son *et al.*,[7] while Suttrop *et al.*[3] claimed much smaller anisotropy with a small longitudinal mass. The theoretical calculation by Käckell and co-workers[28] seems to support the large longitudinal masses.

It is interesting to compare the anisotropy of deduced parameters with those of Mel'nichuk and Pasechnik,[10] who made an analysis similar to the present study. They observed anisotropic IR-reflection spectra in the reststrahlen region for heavily doped 6H–SiC samples ($n_H=1.4\times10^{18}-1.4\times10^{19}$

TABLE III. Best-fit parameters to coupled modes of 6H–SiC.

	Axial mode			Planar mode		
Sample no.	(1)	(2)	(3)	(1)	(2)	(3)
m_H (cm^{-3})	5×10^{16}	4.6×10^{17}	5.6×10^{18}	5×10^{16}	4.6×10^{17}	5.6×10^{18}
ω_p (cm^{-1})	20	70	220	45	140	460
γ (cm^{-1})	40	110	900	90	240	2100
Γ (cm^{-1})	4.8	5.2	5.8	5.4	5.8	6.0
ω_L (cm^{-1})		964.2 (A_{1L})			969.4 (E_{1L})	
ω_T (cm^{-1})		788 (A_{1T})			797 (E_{1T})	
C		0.37			0.22	
ϵ_∞		6.70			6.52	

cm^{-3}) using the electric vector of the incident wave parallel or perpendicular to the c axis, and made a curve-fitting analysis using the plasmon frequency $\omega_p^{\parallel,\perp}$, plasmon damping $\gamma^{\parallel,\perp}$, and phonon damping $\Gamma^{\parallel,\perp}$ as adjustable parameters. They found anisotropy in the plasmon frequency and damping as $\omega_P^{\perp}/\omega_P^{\parallel}\sim2.6$ and $\gamma^{\perp}/\gamma^{\parallel}\sim1.9$, which are comparable to our results.

Let us briefly discuss the errors that occur in deducing the effective masses from the experimental values of the plasma frequency $\omega_p^{\parallel,\perp}$ and the carrier concentration n_H using Eq. (6). The plasma frequency can be determined accurately from the fitting for samples with large carrier concentrations ($\gtrsim5\times10^{17}$ cm^{-3}) as is demonstrated in Fig. 8(c). Here the uncertainty is typically $\pm5\%$. In contrast to the plasmon frequency, the value of n_H may contain large errors because of the ambiguity for the Hall factor r_H. It takes various values depending on the carrier-scattering mechanisms, e.g., $r_H=1.10$, 1.18, and 1.93 for piezoelectric-, acoustic-phonon-, and ionized-impurity scatterings, respectively.[32] However, recent Hall mobility data[33,34] for different carrier concentrations have shown that the temperature dependence of the mobility in α-SiC approaches a $T^{-3/2}$ curve near room temperature. Accordingly, the acoustic-phonon scattering is considered to be the dominant process at room temperature for most of the samples tested in the present work, and our assumption that $r_H=1$ would not cause significant errors in determining the carrier concentration. Actually, in n-type GaP (Ref. 12) and β-SiC (Ref. 16) excellent agreement has been found between the Hall measurement and Raman scattering for carrier concentrations of 10^{16}–10^{18} cm^{-3}, which supports that $r_H\sim1$. In this work we have estimated the accuracy of the effective masses to be $\pm30\%$, considering the error factors of both ω_p and r_H.

TABLE IV. Effective masses in 6H–SiC.

$m_\parallel/m_0$	1.4[a]	0.34[b]	1.5[c]	1.3[d]	1.7[e]	2.0[f]	1.25[g]
$m_\perp/m_0$	0.35[a]	0.24[b]	0.25[c]	0.35[d]	0.25[e]	0.42[i]	0.13, 0.68[g]

[a]This work; Raman scattering.
[b]Suttrop *et al.* (Ref. 3); IR absorption.
[c]Ellis and Moss (Ref. 8); Faraday rotation, IR absorption.
[d]Lomakina and Vodakov (Ref. 9); electrical conductivity.
[e]Mel'nichuk and Pasechnik (Ref. 10); IR reflection.
[f]Son *et al.* (Ref. 7); optically detected cyclotron resonance.
[g]Käckel and co-workers (Ref. 28); band calculation.

By comparing Eq. (6) for the planar and axial modes, the mass anisotropy can be written as

$$m_\parallel/m_\perp=(\epsilon_\infty^{\perp}/\epsilon_\infty^{\parallel})(\omega_p^{\perp}/\omega_p^{\parallel})^2. \tag{7}$$

Here $\omega_p^{\perp}/\omega_p^{\parallel}$ can be directly obtained from the present experiment, therefore, the mass ratio $m_\parallel/m_\perp$ is experimentally determined without ambiguity of r_H or carrier concentration n_H, if $\epsilon_\infty^{\perp}/\epsilon_\infty^{\parallel}$ is known. Thus, the obtained mass anisotropy, $m_\parallel/m_\perp=4.0\pm0.6$ for 6H–SiC and 1.6 ± 0.3 for 4H–SiC, are more reliable than the effective masses themselves.

E. Electron mobility

The drift mobilities of electrons in the direction parallel and perpendicular to the c axis have been calculated from the effective mass and plasmon damping using the equation $\mu^{\parallel,\perp}=e/(m_{\parallel,\perp}\gamma^{\parallel,\perp})$. Figure 12 shows the drift mobility of 4H–SiC against the carrier density n_H. Here, the Hall mo-

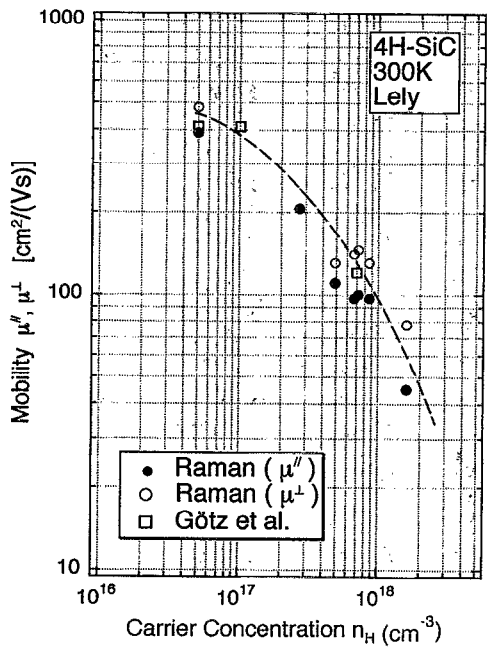

FIG. 12. Drift mobility deduced from Raman scattering (open and solid circles). Hall mobilities by Götz *et al.* (see Ref. 4) are also plotted for comparison. The broken line is drawn to guide the eyes.

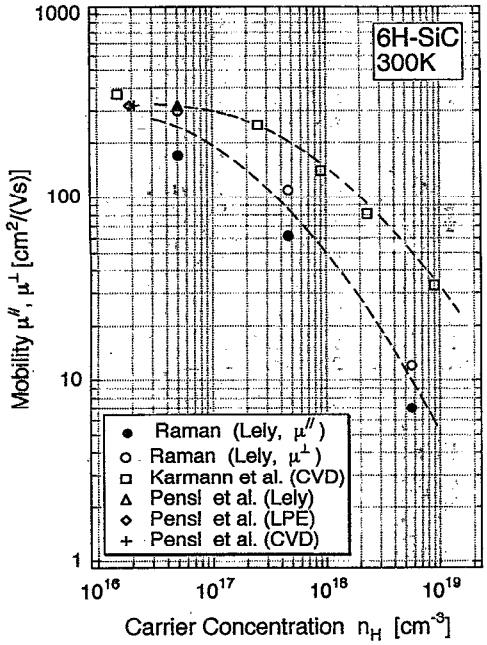

FIG. 13. Drift mobility deduced from Raman scattering (open and solid circles). Hall mobilities by Karmann *et al.* (see Ref. 33) and Pensl and Choyke (see Ref. 34) are also plotted for comparison. The dashed lines are drawn to guide the eyes.

bilities measured by Götz *et al.*[4] for bulk 4H–SiC crystals (grown by a modified Lely method) are also plotted for comparison. Our result is in quantitative agreement with their values within ±30%. Since the Hall mobility μ_H is related to the drift mobility μ by $\mu_H = r_H \mu$, this agreement supports the assumption that the Hall factor r_H is close to unity.

Drift mobilities for 6H–SiC as a function of n_H are shown in Fig. 13 with comparison to recent Hall mobility data from chemical-vapor-deposition (CVD) homoepitaxial layers[33,34] and bulk samples grown by modified Lely and liquid-phase-epitaxy (LPE) methods.[34] Our values obtained for the samples prepared by a modified Lely method are 2–5 times smaller than those of the CVD films at large n_H. This difference is probably due to the superior crystalline quality of the CVD samples.

The deduced mobilities are also anisotropic. The planar component in 4H–SiC is slightly larger than the axial component, $\mu^{\perp}/\mu^{\parallel}=1.2\pm0.3$. This is in contrast with 6H–SiC, where large anisotropy is clearly observed; $\mu^{\perp}/\mu^{\parallel}=2.0\pm0.3$. Lomakina and Vodakov[10] obtained drift-mobility ratios $\mu^{\perp}/\mu^{\parallel}\sim0.9$ for 4H–SiC and ~3 for 6H–SiC from dc resistivity measurements to the directions perpendicular and parallel to the c axis. Recent Hall mobility measurements[2,35] have also shown strong anisotropy for 6H–SiC. Schaffer *et al.*[2] reported $\mu_H^{\perp}/\mu_H^{\parallel}=4.8$ and 0.83 from homoepitaxial layers of 6H– and 4H–SiC, respectively. Schadt *et al.*[35] obtained $\mu_H^{\perp}/\mu_H^{\parallel}=3$–5 for 6H–SiC and 0.8–0.9 for 4H–SiC in bulk samples grown by a modified Lely method. It is concluded from these electrical and Raman experiments that 6H–SiC has large mobility anisotropy when compared with 4H–SiC.

V. SUMMARY

Raman profiles of the LO-phonon–plasmon–coupled modes in n-type 6H– and 4H–SiC bulk crystals with different carrier concentrations have been observed for the planar and axial modes individually. In 4H–SiC there is no discernible difference for the peak intensity and width between these modes, but for the peak shift the planar mode gives a slightly larger value than the axial mode. In 6H–SiC the planar mode shows more remarkable variations with the carrier concentration than the axial mode in the peak intensity and width as well as in the peak shift.

Anisotropic plasmon frequencies and carrier damping constants have been determined from a fitting of theoretical band shape to the observed Raman band profiles. The longitudinal and transverse masses of electrons have been derived from the plasmon frequencies using the carrier concentrations obtained from Hall measurements. The effective mass ratio determined by the present Raman measurement is $m_{\parallel}/m_{\perp}=4.0\pm0.6$ for 6H–SiC and 1.6 ± 0.3 for 4H–SiC. The drift mobility has also been deduced from the Raman analysis. 6H–SiC shows larger mobility anisotropy than 4H–SiC.

ACKNOWLEDGMENTS

The samples used in this work were prepared by several research groups: Advanced Technology Materials, Kyoto Institute of Technology, Nippon Steel, Nissin Steel, Sanyo Electric, Sharp, and Tokyo Tekko. We are grateful to all these groups for providing the samples and Hall data with x-ray-diffraction analyses. We also wish to thank Professor W. J. Choyke and Professor G. Pensl for making available their article prior to publication and for useful discussions.

[1] Landoldt-Börnstein, in *Numerical Data and Functional Relationships in Science and Technology*, edited by O. Madelung (Springer, Berlin, 1986), Vol. 22a.
[2] W. J. Schaffer, G. H. Negley, K. G. Irvine, and J. W. Palmour, Mater. Res. Soc. Symp. Proc. **339**, 595 (1994).
[3] W. Suttrop, G. Pensl, W. J. Choyke, R. Stein, and S. Leibenzeder, J. Appl. Phys. **72**, 3708 (1992).
[4] W. Götz, A. Schöner, G. Pensl, W. Suttrop, W. J. Choyke, R. Stein, and S. Leibenzeder, J. Appl. Phys. **73**, 3332 (1993).
[5] R. Kaplan, R. J. Wagner, H. J. Kim, and R. F. Davis, Solid State Commun. **55**, 67 (1985).
[6] J. Kono, S. Takeyama, H. Yokoi, N. Miura, M. Yamanaka, M. Shinohara, and K. Ikoma, Phys. Rev. B **48**, 10 909 (1993).
[7] N. T. Son, O. Kordina, A. O. Konstantinov, W. M. Chen, E. Sörman, B. Monemar, and E. Janzén, Appl. Phys. Lett. **65**, 329 (1994); N. T. Son, W. M. Chen, O. Kordina, A. O. Konstantinov, B. Monemar, E. Janzén, D. M. Hofman, D. Volm, M. Drechsler, and B. K. Meyer, *ibid.* **66**, 1074 (1995). Note that the ODCR monitors photoluminescence from crystals resulting from thermal perturbations due to absorption of input microwave power.
[8] B. Ellis and T. S. Moss, Proc. R. Soc. London Ser. A **299**, 383 (1967); **299**, 393 (1967). Note that these authors assume that the conduction-band minima are located on the line ΓA in the Brillouin zone.
[9] G. A. Lomakina and Yu. A. Vodakov, Sov. Phys. Solid State **15**, 83 (1973), and references therein.
[10] A. V. Mel'nichuk and Y. A. Pasechnik, Sov. Phys. Solid State **34**, 227 (1992).
[11] M. V. Klein, in *Light Scattering in Solids*, edited by M. Cardona (Springer, Berlin, 1975), p. 147.
[12] G. Irmer, V. V. Toporov, B. H. Bairamov, and J. Monecke, Phys. Status Solidi B **119**, 595 (1983).
[13] G. Irmer, W. Siegel, G. Kühnel, J. Monecke, F. M. M. Yasuoka, B. H. Bairamov, and V. V. Toporov, Semicond. Soc. Technol. **6**, 1072 (1991).

[14] B. H. Bairamov, A. Heinrich, G. Irmer, V. V. Toporov, and E. Ziegler, Phys. Status Solidi B **119**, 227 (1983).
[15] H. Yugami, S. Nakashima, K. Sakai, H. Kojima, M. Hangyo, and A. Mitsuishi, J. Phys. Soc. Jpn. **56**, 1881 (1987).
[16] H. Yugami, S. Nakashima, and A. Mitsuishi, J. Appl. Phys. **61**, 354 (1987). Irmer *et al.* (Ref. 12) have dropped the $\omega^2\Gamma\omega_p^2$ term in the square bracket of the second term in Eq. (2).
[17] For general discussions of pressure induced effects, see, for example, G. Martinez, in *Optical Properties of Solids*, edited by M. Balkanski, *Handbook of Semiconductors*, Vol. 2, series edited by T. S. Moss (North-Holland, Amsterdam, 1980), p. 181.
[18] D. W. Feldman, J. H. Parker, Jr., W. J. Choyke, and L. Patrick, Phys. Rev. **170**, 698 (1968).
[19] D. W. Feldman, J. H. Parker, Jr., W. J. Choyke, and L. Patrick, Phys. Rev. **173**, 787 (1968).
[20] P. J. Colwell and M. V. Klein, Phys. Rev. B **6**, 498 (1972).
[21] M. V. Klein, B. N. Ganguly, and P. J. Colwell, Phys. Rev. B **6**, 2380 (1972).
[22] W. L. Faust and C. H. Henry, Phys. Rev. Lett. **17**, 1265 (1966).
[23] L. Patrick, W. J. Choyke, and D. R. Hamilton, Phys. Rev. **137**, 1515 (1965).
[24] W. J. Choyke and L. Patrick, Phys. Rev. **127**, 1868 (1962).
[25] L. Patrick, Phys. Rev. B **5**, 2198 (1972).
[26] H. G. Junginger and W. van Haeringen, Phys. Status Solidi **37**, 709 (1970).
[27] C. H. Park, B.-H. Cheong, K.-H. Lee, and K. J. Chang, Phys. Rev. B **49**, 4485 (1994).
[28] P. Käckell, B. Wenzien, and F. Bechstedt, Phys. Rev. B **50**, 10 761 (1994). Note the different notations of effective mass components; their $m_{\perp 1}$ corresponds to $m_\parallel$ in this work, while their $m_{\perp 2}$ and $m_\parallel$ correspond to $m_\perp$ in this work.
[29] L. Patrick and W. J. Choyke, Phys. Rev. B **2**, 2255 (1970).
[30] P. T. B. Shaffer, Appl. Opt. **10**, 1034 (1971).
[31] J. F. Scott, T. C. Damen, and J. Shah, Opt. Commun. **3**, 384 (1971).
[32] See, for example, D. L. Rode and S. Knight, Phys. Rev. **3**, 2534 (1971).
[33] S. Karmann, W. Suttrop, A. Schöner, M. Schadt, C. Haberstroh, F. Engelbrecht, R. Helbig, G. Pensl, R. Stein, and S. Leibenzedar, J. Appl. Phys. **72**, 5437 (1992).
[34] G. Pensl and W. J. Choyke, Physica B **185**, 264 (1993), and references therein.
[35] M. Schadt, G. Pensl, R. P. Devaty, W. J. Choyke, R. Stein, and D. Stephani, Appl. Phys. Lett. **65**, 3120 (1994).